VUV Photoionization Cross Sections of HO_2, H_2O_2, and H_2CO

Leah G. Dodson,[1,*] Linhan Shen,[1] John D. Savee,[2] Nathan C. Eddingsaas,[1,†] Oliver Welz,[2,‡] Craig A. Taatjes,[2,*] David L. Osborn,[2,*] Stanley P. Sander,[3] and Mitchio Okumura[1,*]

[1]Department of Chemistry and Chemical Engineering, California Institute of Technology, Pasadena, California 91125, United States

[2]Combustion Research Facility, Sandia National Laboratories, Livermore, California 94551, United States

[3]Jet Propulsion Laboratory, California Institute of Technology, Pasadena, California 91109, United States

Supporting Information

1 Characterization of Instrument Effects using NO_2 Photolysis

Experiments measuring the instrument response function (IRF) used a certified mix of NO_2 in He (Matheson Tri-Gas, 1.00% NO_2 with 0.5% O_2 as a stabilizing agent in He). We conducted NO_2 photolysis experiments at 8 Torr and 10.0 eV photon energy. The NO^+ and NO_2^+ signals are shown in Figure S1. Following photolysis at $t = 0$, we observed a small depletion in the NO_2^+ and a fast rise in the NO^+ signal. The measured depletion of NO_2 (from both photolytic and kinetic reactions) was 4.6 ± 0.5% determined by fitting the data over the time range from −20 to 20 ms. At later

times, a further slight increase in the NO^+ signal and a corresponding decrease in NO_2^+ persisted, which we attributed to the gradient in excimer photolysis energy mentioned earlier. The modeled kinetics (with no modifications) for NO and NO_2 are shown in Figure S1(a) and (b) as green dashed lines.

1.1 Instrument Response Function

The IRF arises from the velocity distribution of the sampled molecule beam and the finite transit time. Taatjes derived a functional form for the response function $h(t)$ for this instrument based on work by Moore and Carr by assuming effusive sampling.[1-2] A Maxwell-Boltzmann velocity spread and finite transit time lead to the following expression for the temporal instrument response function:

$$h(t) \propto \frac{\exp\left(\frac{A}{(t-t_0)^2}\right)}{(t-t_0)^4} \qquad \text{(SE1)}$$

where A and t_0 are fitted constants. Our experiments were carried out at 8 Torr total pressure in He bath gas. The mean free path of the gas molecules in the flow tube was 10–40 μm, while the diameter of the sampling pinhole was 650 μm. The flow through the nozzle was intermediate between molecular and viscous, and we used equation (SE1) empirically.

We determined the IRF from the observed rise of the initial NO formation, shown in Figure S1. The kinetics model predicts that NO rises in the first 0.1 ms to 50% of its final value, whereas the actual 50% rise time is 1 ms. Using MATLAB, we fit the NO^+ rise to the kinetics model curve convolved with the IRF[3-4] described in Equation (SE1) and determined the values for A and t_0 to be -1.2 ms^2 and -0.49 ms, respectively. The instrument response is slower than in previous studies,[3-4] and varied run-to-run (see below for an example of the data from an independent run from the data shown in the main text).

Alternatively to fitting the rise in the NO signal, we could obtain the IRF by fitting the depletion in the NO_2^+ signal (Figure S1(b)), but the inferior signal-to-noise makes the latter option a poor choice.

1.2 Photolysis Gradient

After the initial rise in NO that occurs promptly after photolysis (1 ms 50% rise time, including IRF), the NO is expected to remain constant. Instead, we observe an additional increase in the NO signal of approximately 12% from 10 to 60 ms, as seen in Figure S1(c). Over the same time interval, a linear fit to the NO_2 data (Figure S1(d)) shows a slow depletion of ~0.4% on top of the initial 4.60% depletion due to photolysis. This long-time depletion corresponds to a comparable increase in NO.

We estimated the photolysis gradient from a linear regression of the NO^+ data from 15 to 60 ms. The initial yield of NO was determined using the window from 3–15 ms wherein the NO data are not impacted by the IRF. The slope obtained from the NO rise was 0.23% ms^{-1}.

The IRF and photolysis gradient found for NO and NO_2 are used to define the IRF and photolysis gradient of all other experiments performed here. All time traces were convolved with the IRF to take into account the broadening effects of the instrument. Treatment of the photolysis gradient required a more detailed procedure.

The existence of a photolysis gradient implies that the chemical conditions (i.e. the radical concentrations) vary along the length of the flow tube. If we divide the flow tube into 3.66 mm sections that correspond to 1 ms time windows at our flow velocity of 3.66 mm ms^{-1}, we can map out the effect of changing the initial radical concentration along the length of the flow tube. The radical concentrations measured at (e.g.) 10 ms would correspond to the time evolution of the gas packet initiated 36.6 mm upstream.

The photolysis gradient was incorporated into the kinetic model for NO_2 photolysis by varying the initial radical concentration and simulating the kinetics model in 1 ms steps. Each 1 ms step was combined into one model, which was convolved with the IRF. The red solid lines in Figures S1(c) and S1(d) demonstrate the effect of increasing the initial radical concentration at longer times on the NO and NO_2 modeled kinetics, respectively. Compared to the convolved model without a photolysis gradient (red dashed lines in Figures S1(c) and S1(d)), modeling the kinetics with a photolysis gradient captures both the positive slope in the NO and the negative slope in the NO_2. The negative slope derived from the NO_2 kinetics is in good agreement with the NO linear fit.

2 Deconvolution of Isobaric Signals

We derived the lineshape from the time-of-flight profile for a nominal *m*/*z* with only one species present. For example, H_2CO^+, *m*/*z* = 30.011 is shown in Figure 1(a) (in the text). The lineshape was best described by a Voigt function (with residuals of < 3%); a single Gaussian function gave poorer fits, significantly underpredicting the wings.

Blended peaks were then fit as a sum of two Voigt functions. Figure 1(b) (in the text) shows the fit of the *m*/*z* = 33 peak, which contains contributions from HO_2^+ (at *m*/*z* = 32.998) and $^{13}CH_3OH^+$ (at *m*/*z* = 33.030). Figure 1(c) (in the text) shows fit of the *m*/*z* = 34 peak, which has contributions from $H_2O_2^+$ (at *m*/*z* = 34.005) and $CH_3{}^{18}OH^+$ (at *m*/*z* = 34.030).

We used the fits to identify areas in the time-of-flight distribution that are nearly pure contributions from a single species. For the two nominal *m*/*z* peaks in question (*m*/*z* = 33 and 34), we found that we could take half of each Voigt profile. For example, at *m*/*z* = 33 (Figure 1(b)), the left half (gray hashed area, lower *m/z*) of the HO_2^+ and right half (gray hashed area, higher *m/z*) of the $^{13}CH_3OH^+$ peaks were used. The same procedure was used to separate the $H_2O_2^+$ ion signal

from $CH_3{}^{18}OH^+$ at m/z = 34. Kinetic traces for a given species were obtained by summing over the hashed areas (and renormalizing for peak area) at each kinetic time interval.

3 Absolute Photoionization Cross Section of Methanol

The absolute methanol photoionization spectrum was measured relative to the propene spectrum following the procedure outlined in Welz et al.,[5] and compared to previous reports. The photoionization spectrum of propene is well-known[6] and has been used previously as a reference compound for determining photoionization cross sections.[5,7-8]

Experiments were conducted by introducing propene (2 sccm of 1.00% propene in He) and methanol (1 sccm of 4.667% methanol in He) into the flow tube. Propene was Matheson Tri-Gas, 1.00% in Ar. The total flow was 300 sccm at 4 Torr (balance He). The photon energy was scanned from 10.5–11.5 eV in 0.025 eV increments. We averaged 15 mass spectra for each photon energy. For each photon energy, we measured the integrated intensities of the parent m/z peaks of propene and methanol, summed over 0–60 ms. We then determined the absolute cross sections of methanol $\sigma_{CH_3OH}(E)$ from the ratio of the peak areas using:

$$\sigma_{CH_3OH}(E) = \left(\frac{S_{CH_3OH}(E)}{S_{C_3H_6}(E)}\right)\cdot\left(\frac{[C_3H_6]}{[CH_3OH]}\right)\cdot\left(\frac{\alpha_{C_3H_6}}{\alpha_{CH_3OH}}\right)\cdot\sigma_{C_3H_6}(E) \qquad \text{(SE2)}$$

The absolute photoionization spectrum of methanol is shown in Figure S2. Both the shape and absolute cross sections of the methanol spectrum agree well with the spectrum recorded by Cool, et al., which was also measured relative to propene.[8-9] They assigned a 20% systematic uncertainty in methanol cross sections due to the uncertainty in the cross section of propene.[5] The same 20% systematic uncertainty also applies to our results. We measured the methanol spectrum several times; the scatter in the methanol cross section measurements results in typical cross section errors of ~5%, likely caused by uncertainties in the manometric preparation of the methanol tanks as well

as uncertainties in delivery of the sample to the reaction tube. The CH_3OH cross sections reported in the text (Table 4) reflect the average of several measurements, with total error of ~21%.

Also shown in Figure S2 is the spectrum collected at $m/z = 32$ during the spectrum collection in the $Cl_2/CH_3OH/O_2$ photolysis experiment (scaled to match the CH_3OH spectrum collected above). The methanol spectrum collected during photolysis experiments matches the reference spectrum very well, indicating that observed kinetics depletions at $m/z = 32$ are free of contamination. Also notable is the sharp dip in signal at 11.083 eV in the spectrum obtained during kinetics experiments, which is apparently caused by imperfect normalization to the photon flux. As a consequence, we have removed this data point from the spectra reported in the paper.

4 Experiments 19–22

The photolysis gradient and instrument response function are dependent upon the alignment of the excimer beam as it travels down the flow tube. Experiments 19–22 were conducted using a different excimer alignment. This alignment resulted in a faster rise time. Figures S3(a), S3(b), S3(c) show the kinetic traces for HO_2, H_2O_2, and H_2CO for this data set. The A and t_0 values for this data set were -0.1 ms^2 and -0.1 ms, respectively. The HO_2, H_2O_2, and H_2CO cross sections obtained with this data set are consistent with the cross sections obtained from Experiments 1–18 and have been included in the final evaluation.

5 Highest Occupied Molecular Orbitals of HO_2 and H_2O_2

The HOMO and HOMO-1 of HO_2 and H_2O_2 were investigated at the HF/6-311G level using the Gaussian09[10] suite of programs (UHF/6-311G used for HO_2). The resulting molecular orbitals are shown in Figure S4. With this approach the HOMO of HO_2 is predicted to be the singly occupied 2a″ orbital and the HOMO-1 being the doubly occupied 7a′ orbital, from which electrons can be removed via photoionization to yield the ^{1}A′ and ^{3}A″ cations of HO_2, respectively. Both

ionization processes are expected to contribute to the photoionization cross section over the range of photoionization energies used in the present study. The HOMO and HOMO-1 of H_2O_2 are predicted to be the doubly occupied 4b and 5a orbitals; removal of an electron forms the ^2B and ^2A cations of H_2O_2, respectively. The ^2A cation state is not expected to be accessed until photoionization energies of ~12.6 eV, in slight excess of the range explored in the present work.[11]

Multiple overlapping vibronic states in the near-threshold photoionization of HO_2 and H_2O_2 and highly non-diagonal Franck-Condon factors for the ionization process make it impossible to quantitatively apply the model of Xu and Pratt for estimating photoionization cross sections of free radicals.[12] However, from Figure S4 it is clear that both the HOMO and HOMO-1 of both HO_2 and H_2O_2 are qualitatively similar. As discussed in the main text, the observation of near-threshold photoionization cross-sections that differ by a factor of ~2 is consistent with anticipated orbital occupancy effects predicted by the model for the case where the measured cross-section is dominated by ionization from the singly occupied HOMO of HO_2 or the double occupied HOMO of H_2O_2.

6 Full Kinetics Model

Table S1 shows all minor reactions that were included in the full kinetics model. These reactions, along with the major reactions listed in Table 2 in the text, were used in the Kintecus[13] kinetics modeling program used to fit the data. These reactions played a minor role in the chemistry, but were included mainly to capture any chemistry that could result in radical recycling.

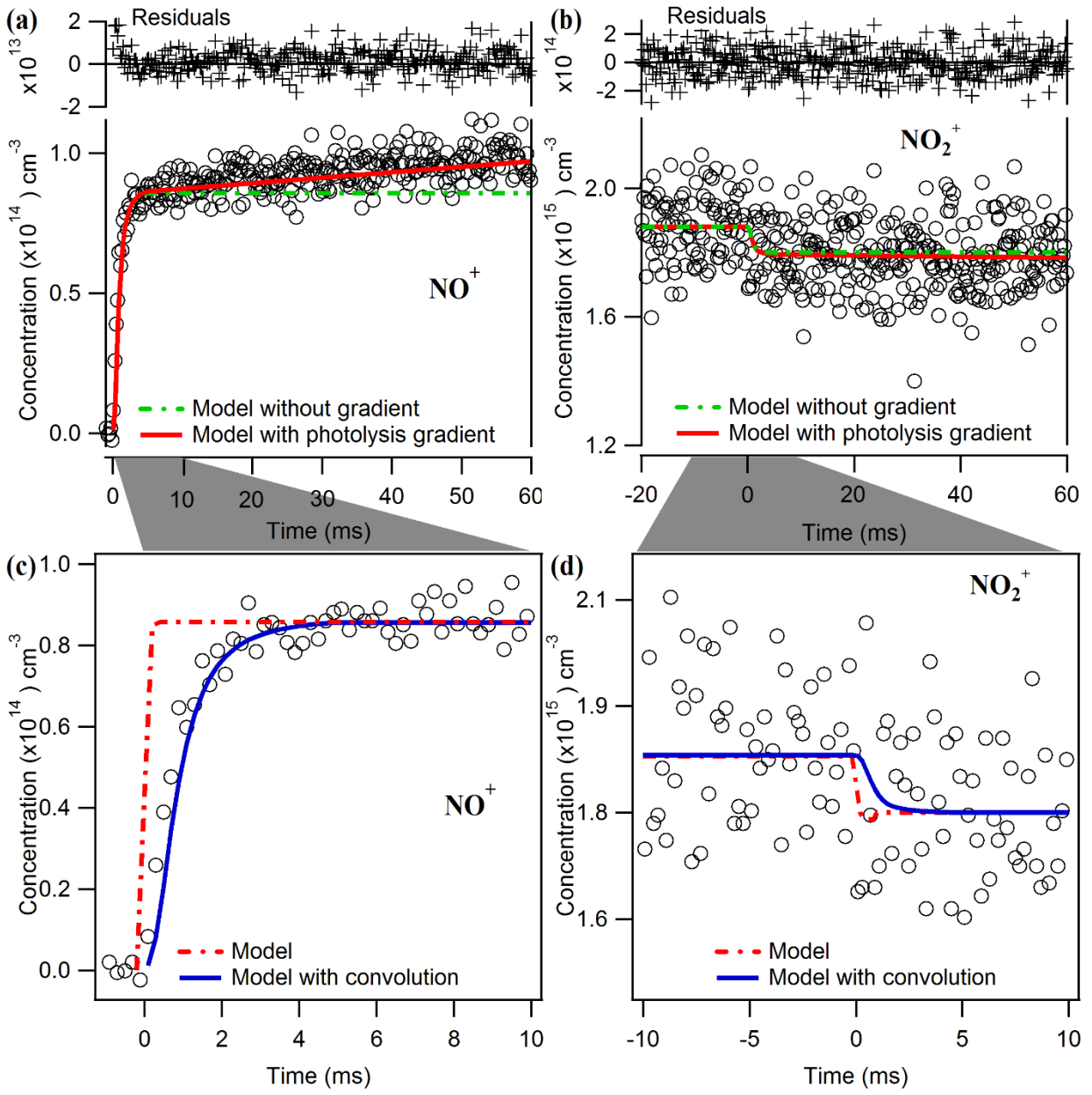

Figure S1. NO_2 photolysis experiments to calibrate instrument effects. Data were scaled to the modeled concentrations as described in the text. (a) Time-dependent NO^+ ion signal at $m/z = 30$, demonstrating the slow rise in NO^+ signal from the photolysis gradient. Unadjusted model (green dash-dot line); Model including photolysis gradient (red solid line). (b) Time-dependent NO_2^+ ion signal at $m/z = 46$, also showing the small change in precursor depletion due to the photolysis gradient. Unadjusted model (green dash-dot line); Model including photolysis gradient (red solid line). (c) NO^+ ion signal zoomed in to early times (0 – 10 ms). Unmodified model (red dash-dot line); Model including linear photolysis gradient, convolved with IRF (blue solid line). (d) NO_2^+ ion signal zoomed in to early times (−10 – 10 ms) Unmodified model (red dash-dot line); Model including linear photolysis gradient, convolved with IRF (blue solid line).

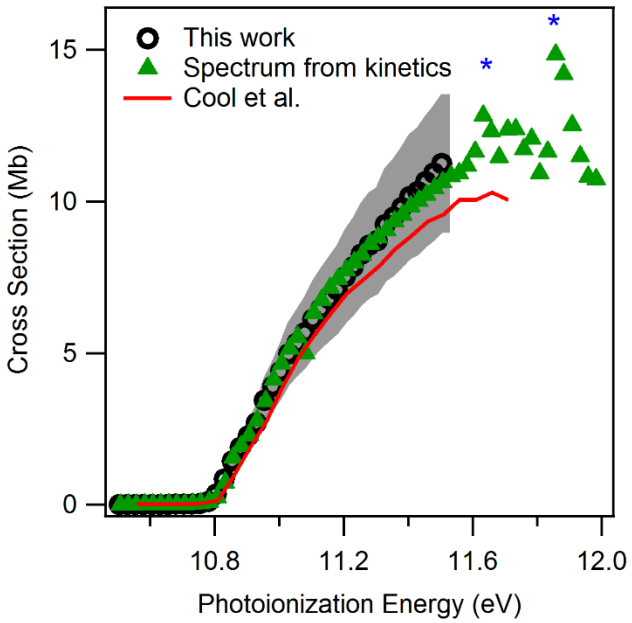

Figure S2. Absolute photoionization cross section of methanol. Literature methanol photoionization spectrum, taken from Cool et al. (red line).[5] Our measured absolute cross section obtained here is shown, the gray shading demonstrates the 20% error associated with referencing the CH_3OH ion signal to the literature propene spectrum. Also shown is the $m/z = 32$ spectrum (triangles) obtained during kinetics experiments described in the paper (scaled relative to our measured reference methanol spectrum). Interferences caused by Ar resonances are indicated by asterisks.

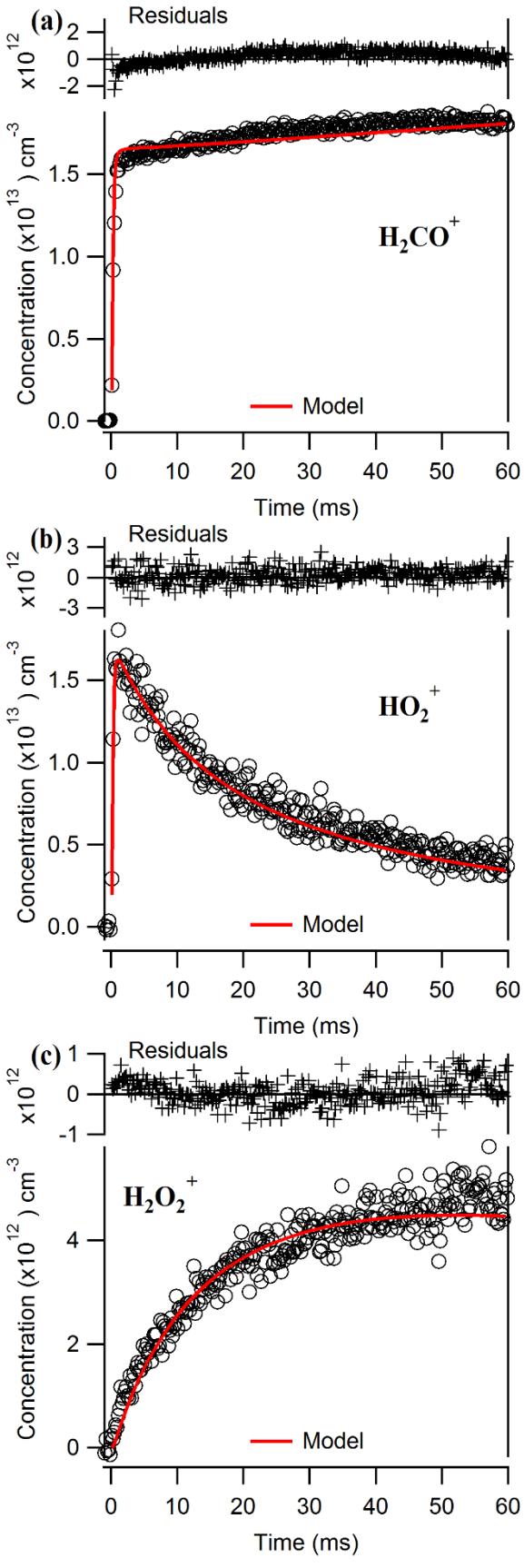
(a)
Residuals
x10^12
2
0
-2
Concentration (x10^13) cm^-3
1.5
1.0
0.5
0.0
H2CO+
Model
0
10
20
30
40
50
60
Time (ms)
(b)
Residuals
x10^12
3
0
-3
Concentration (x10^13) cm^-3
1.5
1.0
0.5
0.0
HO2+
Model
0
10
20
30
40
50
60
Time (ms)
(c)
Residuals
x10^12
1
0
-1
Concentration (x10^12) cm^-3
H2O2+
4
2
0
Model
0
10
20
30
40
50
60
Time (ms)

Figure S3. Single energy kinetics traces for title molecules, from the data set exhibiting a faster rise, indicating a faster IRF. Data are scaled to the model as part of the cross section determination process. Representative time-dependent traces of (a) H_2CO^+, (b) HO_2^+, and (c) $H_2O_2^+$ at 11.45 eV. These data are from Experiment 19 (see Table 3 in the text). The red line is the modeled kinetics of each corresponding trace, convolved with the IRF and including a photolysis gradient and first order wall losses of HO_2 and H_2O_2 (6.6 and 6.9 s^{-1}, respectively).

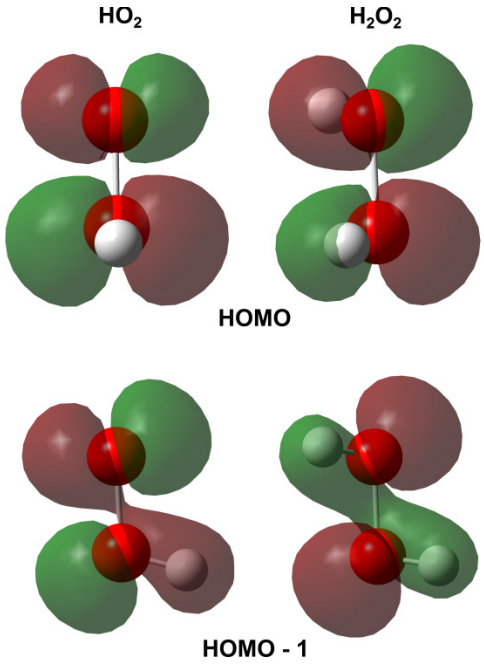

Figure S4. The HOMO and HOMO-1 for HO_2 and H_2O_2 generated using HF/6-311G.

Table S1. Minor reactions that were included in the full kinetics model used to fit data. This table does not include all of the major reactions that were listed in Table 2 in the text. The summation of these two tables represents the full kinetics model. Pressure-dependent rate constants are for 8 Torr. All rate constants are taken from the NASA Data Evaluation[14] unless otherwise noted.

		k_{298K} (cm^3 $molecule^{-1}$ s^{-1})
Hydroxy methyl peroxy reactions		
(12)[a]	$HOCH_2O_2 + HOCH_2O_2 \rightarrow HC(O)OH + HOCH_2OH + O_2$	7.0×10^{-13}
	$HOCH_2O_2 + HOCH_2O_2 \rightarrow HOCH_2O + HOCH_2O + O_2$	5.5×10^{-12}
(13)[a]	$HOCH_2O_2 + HO_2 \rightarrow HOCH_2OOH + O_2$	7.2×10^{-12}
	$HOCH_2O_2 + HO_2 \rightarrow HC(O)OH + H_2O + O_2$	4.8×10^{-12}
(14)[b]	$HOCH_2O + O_2 \rightarrow HC(O)OH + HO_2$	3.5×10^{-14}
HO_2 reactions		
(15)	$H + O_2 \xrightarrow{M} HO_2$	1.1×10^{-14}
(16)	$HO_2 + OH \rightarrow H_2O + O_2$	1.1×10^{-10}
(17)[c]	$HO_2 + ClO \rightarrow HOCl + O_2$	6.9×10^{-12}
OH reactions		
(18)	$OH + OH \xrightarrow{M} H_2O_2$	1.6×10^{-13}
(19)	$OH + OH \rightarrow H_2O + O$	1.8×10^{-12}
(20)	$OH + H_2O_2 \rightarrow HO_2 + H_2O$	1.8×10^{-12}
(21)	$OH + H_2CO \rightarrow HCO + H_2O$	8.5×10^{-12}
(22)	$OH + HCl \rightarrow H_2O + Cl$	7.8×10^{-13}
(23)[c]	$OH + ClO \rightarrow HO_2 + Cl$	1.9×10^{-11}
	$\rightarrow HCl + O_2$	1.2×10^{-12}
(24)	$OH + HOCl \rightarrow H_2O + ClO$	5.0×10^{-13}
(25)[c]	$OH + Cl_2 \rightarrow HOCl + Cl$	6.5×10^{-14}
(26)[c]	$OH + OClO \rightarrow HOCl + O_2$	1.1×10^{-11}
Cl reactions		
(30)[d]	$Cl + CH_2OH \rightarrow HCl + H_2CO$	3.0×10^{-10}
(31)	$Cl + H_2O_2 \rightarrow HCl + HO_2$	4.1×10^{-13}
(32)	$Cl + O_2 \xrightarrow{M} ClO_2$	5.7×10^{-16}
	$ClO_2 \xrightarrow{M} Cl + O_2$	$2.0\times10^{5}(s^{-1})$
(33)	$Cl + ClO_2 \rightarrow Cl_2 + O_2$	2.3×10^{-10}
	$\rightarrow 2ClO$	1.2×10^{-11}
(34)	$ClO + ClO \rightarrow Cl_2 + O_2$	4.8×10^{-15}
	$\rightarrow ClO_2 + Cl$	8.0×10^{-15}
	$\rightarrow OClO + Cl$	3.5×10^{-15}

(35)[c]	$ClO + ClO \xrightarrow{M} Cl_2O_2$	2.3×10^{-15}
	$Cl_2O_2 \xrightarrow{M} ClO + ClO$	$2.7\times10^{-1}(s^{-1})$
(36)[c]	$ClO + OClO \xrightarrow{M} Cl_2O_3$	9.6×10^{-15}
	$Cl_2O_3 \xrightarrow{M} ClO + OClO$	$6.4\times10^{1}(s^{-1})$
(37)	$Cl + OClO \rightarrow ClO + ClO$	5.8×10^{-11}
(38)	$Cl + HOCl \rightarrow Cl_2 + OH$	2.2×10^{-12}
(39)	$Cl + Cl_2O_2 \rightarrow Cl_2 + ClO_2$	1.0×10^{-10}
(40)	$Cl + Cl \xrightarrow{M} Cl_2$	1.4×10^{-14}
Methoxy reactions		
(41)	$CH_3O + O_2 \rightarrow H_2CO + HO_2$	1.9×10^{-15}
(42)[e]	$CH_3O + CH_3O \rightarrow H_2CO + CH_3OH$	1.3×10^{-11}
(43)[f]	$CH_3O + HO_2 \rightarrow H_2CO + H_2O_2$	5.0×10^{-12}
(44)[f]	$CH_3O + OH \rightarrow H_2CO + H_2O$	3.0×10^{-11}

[a]Taken from IUPAC (Volume II).[15] [b]Taken from Veyret et al.[16] [c]Taken from IUPAC (Volume III).[17] [d]Taken from Tyndall et al.[18] [e]Taken from Biggs et al.[19] [f]Taken from Tsang and Hampson.[20]

REFERENCES

1. Taatjes, C. A., How does the Molecular Velocity Distribution Affect Kinetics Measurements by Time-Resolved Mass Spectrometry? *Int. J. Chem. Kin.* **2007,** *39*, 565-570.
2. Moore, S. B.; Carr Jr, R. W., Molecular Velocity Distribution Effects in Kinetic Studies by Time-Resolved Mass Spectrometry. *Int. J. Mass Spectrom. Ion Phys.* **1977,** *24*, 161-171.
3. Welz, O.; Savee, J. D.; Osborn, D. L.; Vasu, S. S.; Percival, C. J.; Shallcross, D. E.; Taatjes, C. A., Direct Kinetic Measurements of Criegee Intermediate (CH_2OO) Formed by Reaction of CH_2I with O_2. *Science* **2012,** *335*, 204-207.
4. Savee, J. D.; Welz, O.; Taatjes, C. A.; Osborn, D. L., New Mechanistic Insights to the $O(^3P)$ + Propene Reaction from Multiplexed Photoionization Mass Spectrometry. *Phys. Chem. Chem. Phys.* **2012,** *14*, 10410-10423.
5. Welz, O.; Zador, J.; Savee, J. D.; Ng, M. Y.; Meloni, G.; Fernandes, R. X.; Sheps, L.; Simmons, B. A.; Lee, T. S.; Osborn, D. L., et al., Low-Temperature Combustion Chemistry of Biofuels: Pathways in the Initial Low-Temperature (550 K-750 K) Oxidation Chemistry of Isopentanol. *Phys. Chem. Chem. Phys.* **2012,** *14*, 3112-3127.
6. Person, J. C.; Nicole, P. P., Isotope Effects in the Photoionization Yields and the Absorption Cross Sections for Acetylene, Propyne, and Propene. *J. Chem. Phys.* **1970,** *53*, 1767-1774.
7. Cool, T. A.; McIlroy, A.; Qi, F.; Westmoreland, P. R.; Poisson, L.; Peterka, D. S.; Ahmed, M., Photoionization Mass Spectrometer for Studies of Flame Chemistry with a Synchrotron Light Source. *Rev. Sci. Instrum.* **2005,** *76*, 094102-7.
8. Cool, T. A.; Wang, J.; Nakajima, K.; Taatjes, C. A.; McLlroy, A., Photoionization Cross Sections for Reaction Intermediates in Hydrocarbon Combustion. *Int. J. Mass Spectrom.* **2005,** *247*, 18-27.
9. Cool, T. A.; Nakajima, K.; Mostefaoui, T. A.; Qi, F.; McIlroy, A.; Westmoreland, P. R.; Law, M. E.; Poisson, L.; Peterka, D. S.; Ahmed, M., Selective Detection of Isomers with Photoionization Mass Spectrometry for Studies of Hydrocarbon Flame Chemistry. *J. Chem. Phys.* **2003,** *119*, 8356-8365.
10. Frisch, M. J.; Trucks, G. W.; Schlegel, H. B.; Scuseria, G. E.; Robb, M. A.; Cheeseman, J. R.; Scalmani, G.; Barone, V.; Mennucci, B.; Petersson, G. A., et al. *Gaussian 09*, Gaussian, Inc.: Wallingford, CT, USA, 2009.
11. Chevaldonnet, C.; Cardy, H.; Dargelos, A., Ab Initio CI Calculations on the PE and VUV Spectra of Hydrogen Peroxide. *Chem. Phys.* **1986,** *102*, 55-61.
12. Xu, H.; Pratt, S. T., Photoionization Cross Section of the Propargyl Radical and Some General Ideas for Estimating Radical Cross Sections. *J. Phys. Chem. A* **2012,** *117*, 9331-9342.
13. Ianni, J. C., A comparison of the Bader-Deuflhard and the Cash-Karp Runge-Kutta integrators for the GRI-MECH 3.0 model based on the chemical kinetics code Kintecus. In *Computational Fluid and Solid Mechanics 2003*, Bathe, K. J., Ed. Elsevier Science Ltd: Oxford, 2003; pp 1368-1372.
14. Sander, S. P.; Abbatt, J.; Barker, J. R.; Burkholder, J. B.; Friedl, R. R.; Golden, D. M.; Huie, R. E.; Kolb, C. E.; Kurylo, M. J.; Moortgat, G. K., et al., Chemical Kinetics and Photochemical Data for Use in Atmospheric Studies, Evaluation Number 17. *JPL Publication 10-6* **2011**.

15. Atkinson, R.; Baulch, D. L.; Cox, R. A.; Crowley, J. N.; Hampson, R. F.; Hynes, R. G.; Jenkin, M. E.; Rossi, M. J.; Troe, J., Evaluated Kinetic and Photochemical Data for Atmospheric Chemistry: Volume II - Gas Phase Reactions of Organic Species. *Atmos. Chem. Phys.* **2006,** *6*, 3625-4055.
16. Veyret, B.; Rayez, J. C.; Lesclaux, R., Mechanism of the Photooxidation of Formaldehyde Studied by Flash Photolysis of Formaldehyde-Oxygen-Nitric Oxide Mixtures. *J. Phys. Chem.* **1982,** *86*, 3424-3430.
17. Atkinson, R.; Baulch, D. L.; Cox, R. A.; Crowley, J. N.; Hampson, R. F.; Hynes, R. G.; Jenkin, M. E.; Rossi, M. J.; Troe, J., Evaluated Kinetic and Photochemical Data for Atmospheric Chemistry: Volume III - Gas Phase Reactions of Inorganic Halogens. *Atmos. Chem. Phys.* **2007,** *7*, 981-1191.
18. Tyndall, G. S.; Orlando, J. J.; Kegley-Owen, C. S.; Wallington, T. J.; Hurley, M. D., Rate Coefficients for the Reactions of Chlorine Atoms with Methanol and Acetaldehyde. *Int. J. Chem. Kin.* **1999,** *31*, 776-784.
19. Biggs, P.; Canosa-Mas, C. E.; Fracheboud, J.-M.; Shallcross, D. E.; Wayne, R. P., Kinetics of the Reaction of F Atoms with CH_3ONO and CH_3O, and the Reaction of CH_3O with a Number of Hydrocarbons. *J. Chem. Soc., Faraday Trans.* **1997,** *93*, 2481-2486.
20. Tsang, W.; Hampson, R. F., Chemical Kinetic Data Base for Combustion Chemistry. Part I. Methane and Related Compounds. *J. Phys. Chem. Ref. Data* **1986,** *15*, 1087-1279.